Engineering with Computers
https://doi.org/10.1007/s00366-023-01909-5

ORIGINAL ARTICLE

A meshfree phase-field model for simulating the sintering process of metallic particles for printed electronics

Zhida Huang[1] · Hao Wang[2] · Lei Chen[3] · Hector Gomez[2] · Bo Li[4] · Changyong (Chase) Cao[1]

Received: 30 May 2023 / Accepted: 25 September 2023

Abstract
Printed electronics are widely used in wearable tech, IoT, and medical devices, and reliable sintering methods are essential for achieving optimal electrode conductivity. However, existing sintering models are often based on trial-and-error or past experience, highlighting the need for a reliable numerical model to improve the process. Traditional phase-field sintering models are limited by factors such as small mesh size requirements, high computational expenses for large-scale simulations, and high mesh sensitivity. In this article, we introduce a new meshfree phase field model based on the recent hot optimal transform meshfree (HOTM) method to simulate nanoparticle sintering processes efficiently and accurately. We use the Galerkin method to develop variational forms for the Cahn–Hillard and the Allen–Chan equation of the phase-field model. In addition, we apply the Local maximum entropy (LEM) shape function to construct a Node-Material Point framework. Finally, we present two efficiency improvement schemes and MPI parallel computation that enable the model to perform large-scale simulations. After several performance tests, we demonstrate its efficiency and accuracy by presenting both 2D and 3D simulation cases in comparison to actual sintering behaviors of the nanoparticles.

Keywords Particle sintering · Meshfree method · Phase-field model · Printed electrodes

1 Introduction

Printed electronics have attracted increasing attention from academia and industry due to their promising merits, including low-cost, scalable manufacturing, compatibility with flexible substrates, ease of integration, and generating less waste [1–3]. In particular, it is suitable for developing large-area flexible and stretchable electronics and energy devices, such as flexible displays, smart labels, animated posters, smart clothing, and human–machine interfaces [4–10]. These electronics are usually developed with printed electrodes from nanoparticle-based inks, which need a post-printing sintering process to enable the high conductivity required for the devices. Currently, most sintering processes in printed electronics are based on the try-and-error method or previous experience and estimation. The optimization step is usually rough and less accurate. To improve the efficiency and effectiveness of the sintering process for nanoparticle-based printed electrodes, a highly efficient numerical model and simulation method is crucial to optimize the sensing conditions for different applications to reduce manufacturing costs and save energy.

The sintering process can be divided into different stages. At the very beginning of the sintering, particles come into contact at specific points. As sintering initiates, these contact points serve as nuclei for interface growth. In addition, the formation of these interfaces will lead to unbalanced sintering traction, causing rapid rigid body motion. Consequently, the vacancy ratio experiences a fast decline. This initial phase is termed the "initial sintering stage." As particles arrange themselves into a structure where most experiences balanced rigid body forces, the sintering process transitions into a phase of consistent, steady progress known as the "steady sintering stage." During this phase, the reduction in vacancy ratio is primarily driven by solid diffusion, which

✉ Changyong (Chase) Cao
ccao@case.edu

[1] Department of Mechanical and Aerospace Engineering, Case Western Reserve University, Cleveland, OH 44106, USA

[2] School of Mechanical Engineering, Purdue University, West Lafayette, IN 47907, USA

[3] Department of Mechanical Engineering, The University of Michigan-Dearborn, Dearborn, MI 48128, USA

[4] Department of Engineering Mechanics, Peking University, Beijing 110084, China

Published online: 31 October 2023

occurs at a slower pace compared to the initial stage [11, 12]. From a thermodynamic point of view, the main driving effect of the sintering process is the release of the surface energy of the material, which is a positively correlated function of local curvature. Therefore, the sintering phenomena can be explained as the system thermodynamic behavior being elevated by the increased temperature and the system energy tending to minimize itself, which will lead to the internal mass migration that lowers the overall surface energy. The specific observations of the mass migration include the vanishing of small surface texture, forming of the dihedral angle on the boundary of interfaces, and small particles fast merging into large ones. In addition, a fraction of the released surface energy is transferred to interface bonding, where interparticle sintering stress is generated. Many factors control the sintering process, including surface energy, interface energy, temperature, and the shape of the particles [13–15]. The numerical model should be able to simulate the above sintering behaviors accurately and efficiently.

The earliest numerical works were mainly based on the constitutive relation between local surface curvature and diffusion advection [11, 16–19]. Inspired by those works, various improved methods were proposed. For example, the Molecular Dynamic (MD) simulation is one of the most widely used approaches to study the sintering process [20–24]. In this method, the surface energy is expressed by explicitly simulating every atom of the particles, thus, the MD model is only suitable to study local interface necking or sintering of a limited number of particles due to the constraint of computational power. Discrete-element method (DEM) simplifies each particle in the model to a separate spherical node that interacts with one another [25–27]. Since the sintering stress was related to particle distance, the shape of the particles could only be a sphere in their model, limiting the accuracy of the particle morphology. Besides those methods, some non-physical-constitutive-based methods such as Cellular Automata and Monte-Carlo were also developed to mimic the sintering behaviors [28–30].

Compared with the above models, the phase-field sintering model has demonstrated promising performance in solving this problem. Jing et al. [31] proposed the first phase-field sintering model, in which the form of free energy in terms of both order parameters and concentration was proposed. Wang et al. [32] further introduced rigid body motion into the computation model. Chockalingam et al. [33] investigated the influence of the coefficients in the governing equations. They suggested that the solid diffusion coefficient should obey the Arrhenius equation, and then investigated how the temperature change and size ratio affected the simulation using two-particle sintering cases. The scale of the geometry is proportional to the total number of particles N_p. In addition, the number of governing equations equals to $N_p + 1$. Therefore, the overall computation expense is $O({N_p}^2)$, which makes it difficult to perform large-scale simulations. In addition, Termuhlen et al. [34] reported a simulation work based on Wang's model [32], in which they used a technique that a cutoff range is defined for the particles with the same phase so that the N_p can be limited, thus large-scale simulation is possible. This approach might damage the robustness of the model since the cutoff range condition depends on the problem and may not be assured when the geometry changes. Hötzer [35] presented a large-scale model simulating green body sintering, in which chemical potential and temperature are coupled.

The phase-field model may be implemented within the framework of finite-difference method (FDM), finite-element method (FEM), and many others. Tonks et al. [36] proposed an adaptive discretization scheme dedicated to phase-field models with structured mesh. However, due to the small scale of phase interface and boundary thickness compared to the geometry, ideally the global mesh size for phase-field models must be close to the boundary thickness in the standard FEM or FDM scheme, which leads to high computation intensity and mesh sensitivity. In fact, when using FEM, the development of the diffusion boundary can vary for structured meshing with different textures, even if the mesh size is the same [37]. To address these issues, meshfree methods provide a flexible spatial discretization scheme [38]. In this study, we are inspired by the hot optimal transform meshfree (HOTM) method [39–43] and propose a meshfree phase-field sintering model using the node-material point framework implemented in HOTM. In this method, we adopt two sets of points, material points and nodes, for the spatial discretization of the problem domain. The order parameters and concentration of solid and vacancy phases are defined at the nodes, while driving forces are computed on the material points. This framework employs the local maximum entropy (LME) shape function, which has a tunable nodal search range to initialize the connectivity map among material points and nodes accordingly. The LME shape function is an accurate and robust approximation scheme [44, 45], which has been verified for phase-field interface problems [46, 47]. Furthermore, we employ the Gaussian-based LME shape function, which enables high-order approximation of nonlinear functions with reduced amount of nodes. On the other hand, to achieve accurate predictions of vacancy distribution and porosity in printed electronics, a substantial number of particles must be simulated, demanding highly efficient computational schemes. We presented two efficiency improvement methods to overcome this challenge. One method reduces computation intensity by leveraging the LME material point framework, while the other handles

the computation complexity of problems involving a large number of particles.

This paper is organized as follows: the governing equation of the model is first introduced, followed by the explanation of spatial discretization and time discretization. The two efficiency improvement methods are then presented. After that, the model is verified by testing the sintering necking of two particles. Finally, the sintering behaviors of both 2D and 3D cases are evaluated and discussed in comparison with experimental observation.

2 Numerical model

2.1 Governing equations

In this work, we adopt Wang's model [32] as the base model. The variable to be solved is defined as $\boldsymbol{\eta} \in R^{N_\mathrm{p}}$ the order parameters, and $\rho \in R^1$ the concentration, which are continuously changing over the computation domain. The concentration ρ represents the spatial state of either solid or vacancy, 1 for solid, and 0 for vacancy. The order parameter $\boldsymbol{\eta}$, essentially a vector with dimension equal to the number of particles, stands for the spatial state of phase. In this work, $\eta(\alpha), \alpha = 1, 2, \ldots, N_\mathrm{p}$ is used to denote the α-th element of $\boldsymbol{\eta}$. In addition, the order parameters can be written as $\boldsymbol{\eta} = \begin{bmatrix}\eta(1) & \eta(2) & \ldots & \eta(N_\mathrm{p})\end{bmatrix}$. $\eta(\alpha) = 1$ stands for the position being occupied by the α-th particle (Fig. 1). The sintering model depicts the system free energy F as

$$F(\boldsymbol{\eta}, \rho) = \int \left[f(\boldsymbol{\eta}, \rho) + \frac{1}{2}\kappa_\rho |\nabla \rho|^2 + \frac{1}{2}\sum_{\alpha=1}^{N_\mathrm{p}} \kappa_\eta |\nabla \eta(\alpha)|^2 \right] \mathrm{d}^3 r, \tag{1}$$

where the inner free energy density f is

$$\begin{aligned} f(\boldsymbol{\eta}, \rho) =& A\rho^2(1-\rho^2) + B\left[\rho^2 + 6(1-\rho)\sum_\alpha \eta(\alpha)^2 - \right. \\ & \left. 4(2-\rho)\sum_\alpha \eta(\alpha)^3 + 3\left(\sum_\alpha \eta(\alpha)^2\right)^2\right], \end{aligned} \tag{2}$$

where κ_ρ and κ_η are the boundary coefficients for concentration and order parameters, respectively. In the expression of $f(\boldsymbol{\eta}, \rho)$, A, B are constant coefficients.

The governing equations of the two types of variables are descriptions of their driving force, i.e., the time derivative. The governing equation of the order parameter η is referred as Allen–Cahn equation, while the one of concentration ρ is referred as Cahn–Hillard equation. The model further considers the rigid body motion. An extra velocity representing body motion is introduced. Therefore, the governing equations are

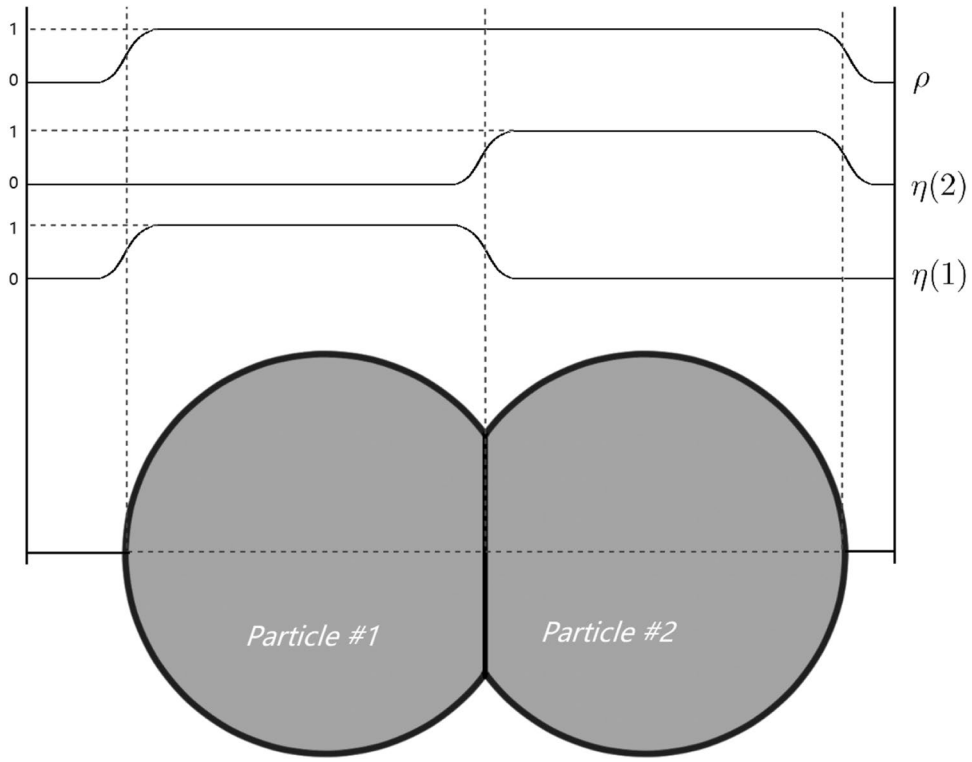

Fig. 1 Schematic diagram of the concentration and order parameter distribution along the center line. The concentration and order parameters are continuous variables. Along the normal direction on the boundary or the interface, the values of concentration and order parameters change smoothly from one state to another accordingly

$$\frac{\partial \rho}{\partial t} = \nabla \cdot \left(D(\boldsymbol{\eta}, \rho) \nabla \frac{\delta F(\boldsymbol{\eta}, \rho)}{\delta \rho} - \rho \boldsymbol{v}_{\text{adv}} \right), \tag{3}$$

and

$$\frac{\partial \eta(\alpha)}{\partial t} = -L \frac{\delta F(\boldsymbol{\eta}, \rho)}{\delta \eta(\alpha)} - \nabla \cdot [\eta(\alpha) \boldsymbol{v}_{\eta,\text{adv}}(\alpha)], \tag{4}$$

where L is the boundary mobility constant, and $D(\eta, \rho)$ is the concentration diffusion coefficient. It is defined by

$$\begin{aligned} D(\boldsymbol{\eta}, \rho) =& D_{\text{vol}} \Phi(\rho) + D_{\text{vap}}[1 - \Phi(\rho)] + D_{\text{surf}} \rho(1 - \rho) + \\ & D_{\text{gb}} \sum_{\alpha} \sum_{\alpha \neq \alpha'} \eta(\alpha) \eta(\alpha'), \end{aligned} \tag{5}$$

where D_{vol}, D_{vap}, D_{surf}, and D_{gb} are diffusivity for solid, vapor, surface, and interface, respectively, and $\Phi(\rho) = \rho^3(10 - 15\rho + 6\rho^2)$.

In Eqs. (3) and (4), $\boldsymbol{v}_{\text{adv}} \in R^3$ and $\boldsymbol{v}_{\eta,\text{adv}}(\alpha) \in R^3$ are the rigid body motion advection velocities. The velocities are generated due to the interface force, which will apply force and torque to the particles. The volumetric sintering force density is

$$\boldsymbol{b}(\alpha) = k \sum_{\beta \neq \alpha} (\rho - \rho_0) \langle \eta(\alpha), \eta(\beta) \rangle [\nabla \eta(\alpha) - \nabla \eta(\beta)], \tag{6}$$

where

$$\langle \eta(\alpha), \eta(\beta) \rangle = \begin{cases} 1 & \text{if} \quad \eta(\alpha)\eta(\beta) > c, \\ 0 & \text{else.} \end{cases} \tag{7}$$

In Eqs. (6) and (7), ρ_0 is the characterized grain boundary density, k is the stiffness coefficient, and c is the order parameter threshold. The setting of these coefficients ensures that only the particle interfaces contribute to the sintering force. The force and torque applied on the α-th particle is then solved as

$$\boldsymbol{F}(\alpha) = \int_{\Omega} \boldsymbol{b}(\alpha) \mathrm{d}r^3, \tag{8}$$

$$\boldsymbol{T}(\alpha) = \int_{\Omega} [\boldsymbol{r} - \boldsymbol{r}(\alpha)] \times \boldsymbol{b}(\alpha) \mathrm{d}r^3. \tag{9}$$

Here, $\boldsymbol{r}(\alpha) = \int_{\Omega} \boldsymbol{r} \eta(\boldsymbol{r}, \alpha) \mathrm{d}r^3 / V(\alpha)$ is the position of the center of α-th particle, where $V(\alpha)$ is the volume of the particle. The rigid body motion advection velocity is obtained by overlapping two advection velocity fields which are proportional to the sintering force and torque:

$$\begin{aligned} \boldsymbol{v}_{\eta,\text{adv}}(\boldsymbol{r}, \alpha) =& \frac{1}{V(\alpha)} \Big[m_t \boldsymbol{F}(\alpha) + m_r \boldsymbol{T}(\alpha) \\ & \times \Big[\boldsymbol{r} - \boldsymbol{r}(\alpha) \Big] \Big] \eta(\boldsymbol{r}, \alpha), \end{aligned} \tag{10}$$

where m_t and m_r are mobility constants for force and torque, respectively. The concentration advection velocity is then solved as

$$\boldsymbol{v}_{\text{adv}}(\boldsymbol{r}) = \sum_{\alpha} \eta(\alpha) \boldsymbol{v}_{\eta,\text{adv}}(\boldsymbol{r}, \alpha). \tag{11}$$

Since Eq. (3) is a conserved equation of concentration, a flux potential of concentration can be defined as

$$\mathcal{W}(\boldsymbol{\eta}, \rho) = \frac{\delta F(\boldsymbol{\eta}, \rho)}{\delta \rho} = \frac{\partial f(\boldsymbol{\eta}, \rho)}{\partial \rho} - \kappa_{\rho} \nabla^2 \rho. \tag{12}$$

Then, Eq. (3) is rewritten as

$$\frac{\partial \rho}{\partial t} = \nabla \cdot (D(\boldsymbol{\eta}, \rho) \nabla \mathcal{W}(\boldsymbol{\eta}, \rho) - \rho \boldsymbol{v}_{\text{adv}}). \tag{13}$$

The weak form of the governing equations is then derived. The standard Ritz–Galerkin method is employed for the proposed phase-field model. We first define the bilinear forms for arbitrary spatial scalar g and vector v as

$$\begin{cases} < g, \phi >= \int_{\Omega} g \phi \mathrm{d}v, \\ < \mathbf{v}, \nabla \phi >= \int_{\Omega} \mathbf{v} \cdot \nabla \phi \mathrm{d}v \end{cases} \tag{14}$$

where $\phi \in H^1(\Omega)$ is the test function for scalar. $H^1(\Omega)$ is the classical Sobolev Space. Combined with Eqs. (1) and (2), Eqs. (13) and (4) are then reformatted as

$$\left\langle \frac{\partial \rho}{\partial t}, \phi_{\rho} \right\rangle + < D \nabla \mathcal{W}, \nabla \phi_{\rho} > - < \rho \boldsymbol{v}_{\text{adv}}, \nabla \phi_{\rho} >= 0, \tag{15}$$

and

$$\begin{aligned} & < \frac{\partial \eta(\alpha)}{\partial t}, \phi_{\eta}(\alpha) > + < L \frac{\partial f}{\partial \eta(\alpha)}, \phi_{\eta}(\alpha) > + < L \kappa_{\eta} \nabla \eta(\alpha) \\ & \quad - \eta(\alpha) \boldsymbol{v}_{\eta\text{adv}}(\alpha), \nabla \phi_{\eta}(\alpha) >= 0, \end{aligned} \tag{16}$$

where ϕ_{ρ} and $\phi_{\eta}(\alpha)$ are the test functions for ρ and $\eta(\alpha)$, respectively. Equations (15) and (16) are the weak forms of the system. It should be noted that when initializing the geometry, enough space is left between the particles and the boundary of the computation area to prevent them from contacting each other. In the applications presented in this work, no material is transferring through the boundary of the computational domain, so the insulation, i.e., zero-flux, boundary condition is applied to the geometry boundaries.

2.2 Spatial discretization

This work employed the same spatial discretization scheme introduced within the HOTM framework, i.e.,

the node-material point framework based on the local maximum entropy (LME) approximation [48]. The computational domain is discretized into two sets of points, material points and nodes. Within the original HOTM framework, the parameters related to geometry, such as displacement, velocity, and acceleration are stored at nodes, while the material properties, strains and stress are carried by material points. In this particular application, the computational domain is fixed, and the particles move due to the sintering in the domain. Thus, we made the according modifications. The problem variables, including the order parameters and phase concentration, are stored on each node, while the material points only serve as integration points to calculate the driving forces. We denote the LME shape function of a-th node with $N_a(x)$, and the material point index as p. Since the LME shape function possesses the property of Gaussian decay [44], a search range h_a is set for interpolating node value to the material point, beyond which the shape function $N_a(x)$ is considered to be zero. The search range takes form as $h_a = h\sqrt{-\log(\delta_0)}\gamma_a$, where h is the nodal spacing, γ a controllable parameter, and δ_0 the cutoff tolerance. Then, for each material point, a domain $N_H(x_p) = \{x_a \in \mathcal{M}_p : |x_a - x_p| \leq h_a\}$ is defined which contains all the contributing nodes. The discretization scheme is shown in Fig. 2. Therefore, the values and gradient of order parameters and concentration on material points are approximated as

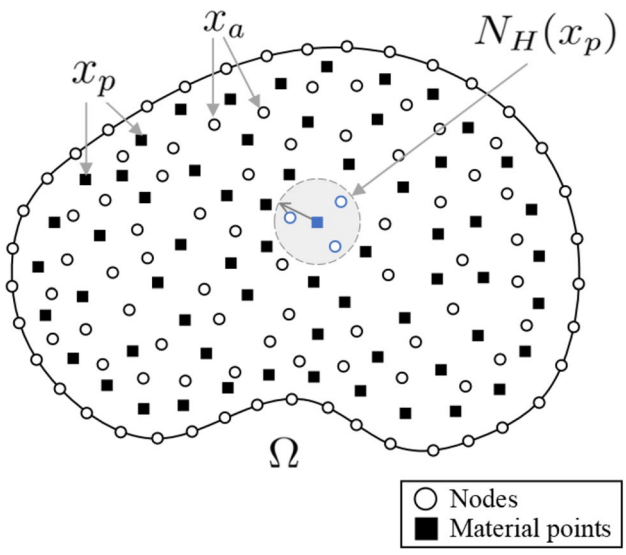

Fig. 2 Schematic of the node-material-points framework. The order parameters $\boldsymbol{\eta}$ and concentration ρ are stored on the nodes. The values of $\boldsymbol{\eta}$ and ρ are interpolated at the material point x_p using the values on the nodes within the search range $N_H(x_p)$. Then, the driving forces are solved on the material points

$$\begin{cases} \eta_p(\alpha) = \sum\limits_{a\in\mathcal{A}_p} \eta_a(\alpha) N_a(x_p), \\ \rho_p = \sum\limits_{a\in\mathcal{A}_p} \rho_a N_a(x_p), \\ \nabla\eta_p(\alpha) = \sum\limits_{a\in\mathcal{A}_p} \eta_a(\alpha) \nabla N_a(x_p), \\ \nabla\rho_p = \sum\limits_{a\in\mathcal{A}_p} \rho_a \nabla N_a(x_p), \end{cases} \tag{17}$$

where $\mathcal{A}_p$ denotes that all indices of node inside $N_H(x_p)$.

The bilinear form Eq. (14) is then written as

$$\begin{cases} < g, \phi > \approx \sum\limits_{p} \sum\limits_{a\in\mathcal{A}_p} w_p g_p \phi_a N_a(x_p), \\ < \mathbf{v}, \nabla\phi > \approx \sum\limits_{p} \sum\limits_{a\in\mathcal{A}_p} w_p \phi_a \mathbf{v}_p \cdot \nabla N_a(x_p) \end{cases} \tag{18}$$

where w_p is the weight of the material point. On the right-hand-sides of Eqs. (15), and (16), the integration is then solved using the weighted summation of the solved value on material points as shown in Eq. (14). With this setup, the weak form Eqs. (15) and (16) are rewritten into spatial discretized form as

$$\left(\frac{\partial\rho}{\partial t}\right)_a = \mathcal{F}_{\rho,a}, \quad \left(\frac{\partial\eta(\alpha)}{\partial t}\right)_a = \mathcal{F}_{\eta,a}(\alpha), \tag{19}$$

where

$$\begin{aligned} \mathcal{F}_{\rho,a} = \frac{1}{m_a} \sum_{p\in\mathcal{M}_a} w_p \big[& -D_{p,n} \nabla N_{a,p} \cdot \nabla \mathcal{W}_p \\ & + \rho_{n,p} \nabla N_{a,p} \cdot \boldsymbol{v}_{\text{adv},p} \big], \end{aligned} \tag{20}$$

$$\begin{aligned} \mathcal{F}_{\eta,a}(\alpha) = \frac{1}{m_a} \sum_{p\in\mathcal{M}_a} w_p \Bigg[& -L N_{a,p} \left(\frac{\partial f}{\partial \eta(\alpha)}\right)_p + \nabla N_{a,p} \\ & \cdot (-L\kappa_\eta \nabla\eta_p(\alpha) + \\ & \eta_p(\alpha) \boldsymbol{v}_{\eta,\text{adv},p}(\alpha)) \Bigg]. \end{aligned} \tag{21}$$

In Eqs. (20) and (21), $\mathcal{M}_a$ is a set of material points such that node a is inside its search range,

$$m_a = \sum_{p\in\mathcal{M}_a} w_p N_a(x_p), \tag{22}$$

is the nodal lumped volume, and

$$\nabla\mathcal{W}_p = \sum_{a\in\mathcal{A}} \mathcal{W}_a \nabla N_a(x_p), \tag{23}$$

is the concentration potential gradient on the material points where

$$\mathcal{W}_a = \frac{1}{m_a} \sum_{p \in \mathcal{M}_a} w_p \left[N_{a,p} \left(\frac{\partial f}{\partial \rho} \right)_p + \kappa_\rho \nabla N_{a,p} \cdot \nabla \rho_p \right]. \tag{24}$$

To solve the material point rigid body advection velocities $\boldsymbol{v}_{\mathrm{adv},p}$ and $\boldsymbol{v}_{\eta,\mathrm{adv},p}(\alpha)$), Eqs. (6) to (11) need to be discretized. Under the current framework, Eqs. (8) and (9) are solved by accumulating the material point value as

$$\boldsymbol{F}(\alpha) = \sum_p w_p \boldsymbol{b}_p(\alpha), \tag{25}$$

$$\boldsymbol{T}(\alpha) = \sum_p w_p \left[\boldsymbol{r}_p - \boldsymbol{r}(\alpha) \right] \times \boldsymbol{b}_p(\alpha), \tag{26}$$

where

$$\boldsymbol{b}_p(\alpha) = k \sum_{\beta \neq \alpha} (\rho_p - \rho_0) \left\langle \eta_p(\alpha), \eta_p(\beta) \right\rangle \left[\nabla \eta_p(\alpha) - \nabla \eta_p(\beta) \right], \tag{27}$$

is the material point sintering body force density. Then, the form of material point rigid body advection velocities are solved as

$$\boldsymbol{v}_{\eta,\mathrm{adv},p}(\alpha) = \frac{1}{V(\alpha)} \left[m_t \boldsymbol{F}(\alpha) + m_r \boldsymbol{T}(\alpha) \times \left[\boldsymbol{r} - \boldsymbol{r}(\alpha) \right] \right] \eta_p(\alpha), \tag{28}$$

and

$$\boldsymbol{v}_{\mathrm{adv},p}(\alpha) = \sum_\alpha \eta_p(\alpha) \boldsymbol{v}_{\eta,\mathrm{adv},p}(\alpha). \tag{29}$$

The derivative of the inner energy density in terms of concentration and potential in Eqs. (20) and (21) are

$$\begin{aligned} \left(\frac{\partial f}{\partial \eta(\alpha)} \right)_p =& 12B \Big[(1 - \rho_p) \eta_p(\alpha) - (2 - \rho_p) \eta_p^2(\alpha) \\ &+ \eta_p(\alpha) \sum_\beta \eta_p^2(\beta) \Big], \end{aligned} \tag{30}$$

$$\begin{aligned} \left(\frac{\partial f}{\partial \rho} \right)_p =& A(4\rho_p^3 - 6\rho_p^2 + 2\rho_p) + B \Bigg(2\rho_p - 6 \sum_\alpha \eta_p(\alpha)^2 \\ &+ 4 \sum_\alpha \eta_p(\alpha)^3 \Bigg). \end{aligned} \tag{31}$$

Equations (21) and (20) are the discretized nodal driving force. Equation (17) can be simply substituted into Eqs. (16) to (31), so the nodal driving forces are essentially the functions of nodal order parameters and concentration.

2.3 Time discretization

Since the RHS of Eqs. (15) and (16) are high-order nonlinear in terms of the order parameters, an explicit second-order Runge–Kutta method is employed for accurate and efficient time discretization. The current time is denoted as t^n. Combined with the spatial discretization scheme, the fully discretized equations are yielded as

$$\begin{cases} \eta_a^{n+\frac{1}{2}}(\alpha) = \eta_a^n(\alpha) + \frac{1}{2} \mathcal{F}_{\eta,a}^n(\alpha) \Delta t, \\ \rho_a^{n+\frac{1}{2}} = \rho_a^n + \frac{1}{2} \mathcal{F}_{\rho,a}^n \Delta t, \\ \eta_a^{n+1}(\alpha) = \eta_a^{n+\frac{1}{2}}(\alpha) + \frac{1}{2} \mathcal{F}_{\eta,a}^{n+\frac{1}{2}}(\alpha) \Delta t, \\ \rho_a^{n+1} = \rho_a^{n+\frac{1}{2}} + \frac{1}{2} \mathcal{F}_{\rho,a}^{n+\frac{1}{2}} \Delta t, \end{cases} \tag{32}$$

where $t^{n+\frac{1}{2}}$ denotes an internal time between t^n and t^{n+1} introduced by second-order Runge–Kutta. $\mathcal{F}_{\eta,a}^n$, $\mathcal{F}_{\rho,a}^n$, $\mathcal{F}_{\eta,a}^{n+\frac{1}{2}}$, and $\mathcal{F}_{\rho,a}^{n+\frac{1}{2}}$, the driving force on t^n and $t^{n+\frac{1}{2}}$, are solved by substituting the nodal value of concentration and order parameters on the corresponding time step into Eqs. (20) and (21). Lee et al. proposed a stable criterion of the maximum time step length for diffusion problems [49], which implies that our algorithm is stable when $\Delta t \leq d_{min}^2/(2L\kappa_\eta)$, where Δt is the time step, and d_{min} is the global minimum nodal distance. To ensure the stability of our implementation, we take 1/10 of the calculated value as the time step.

2.4 Meshfree efficiency improvement

In classical FEM or FDM, the mesh size for simulation is required to be small enough to capture the phase boundary and interfaces accurately. During the simulation, the boundaries and interfaces are possible to develop at any position of the geometry, thus, the small mesh size requirement is applied globally, which largely increases the computational cost. As a result, traditional FEM or FDM often struggle with resource-intensive problems in phase-field models. To overcome this shortcoming, we present a meshfree efficiency improvement method, which takes advantage of the properties of the LME material point framework.

In Eq. (17), the order parameters and concentration and their gradients $\eta_p(\alpha), \rho_p, \nabla \eta_p(\alpha), \nabla \rho_p$ of a certain material point p are solved using the nodal values from only the corresponding contributing node set $\mathcal{A}_p$. The driving force is solved using only material point information as input in Eqs. (20) and (21). However, when all nodal values within $\mathcal{A}_p$ are equal, the spatial gradient of the variables at the material point $\nabla \eta_p(\alpha), \nabla \rho_p$ vanishes, resulting

in the right-hand sides of Eqs. (21) and (20) to be zero. This case corresponds to the state of $\mathcal{A}_p$ completely contained in the vacancy or inner particle area, where the calculation of driving force gives trivial solutions.

Based on the above observation, we present the following efficiency improvement scheme. When the value of $\nabla\eta_p(\alpha)$ and $\nabla\rho_p$ are solved using Eq. (17) on the beginning of each timestep, iterate through the material points to check if $||\nabla\boldsymbol{\eta}_{p,n}|| < \epsilon_\eta$ and $|\nabla\rho_p| < \epsilon_\rho$, where ϵ_η and ϵ_ρ are two given tolerances. If both of them are smaller than the tolerance, the material point is then deactivated and the solution on it will be skipped. Ideally, the material points at the vacancy or inner particle areas are deactivated, while only those near the interface and boundary are activated, where the gradient of η and ρ are non-zero. This leads to a significant acceleration of the calculation. Furthermore, since only a small fraction of material points are activated, more material points can be initialized, and a smaller search range can be employed, thereby improving accuracy.

2.5 Efficiency improvement of the order parameters

In the phase-field sintering model, the nodal degree of freedom is $N_\mathrm{p}+1$. Assuming a constant N_0, the average number of nodes contained in a single particle for a given average node spacing, the total number of nodes required for N_p particles is $N_\mathrm{p}\times N_0$. As a result, the system degree of freedom is $O\big((N_\mathrm{p}+1)\times N_\mathrm{p}\times N_0\big)$. This leads to a computational complexity proportional to N_p^2, which poses a significant challenge when simulating large numbers of particles.

However, it is noticed that a certain phase α, if $\eta(\alpha)=0$, does not contribute to the driving force solution for any phase. Furthermore, in the vacancy area, all order parameters are zero, while in the inner particle area, only one order parameter is non-zero. In addition, the number of non-zero phases on the boundary or interface is less than three. Based on this observation, we propose the following efficiency improvement method: After solving Eq. (17), pass only the non-zero phases in $\boldsymbol{\eta}$ to Eqs. (21) and (20), so that only the relevant phases are solved and all other trivial solutions are skipped. This is achieved by defining order parameters as key-value maps with overloaded algebraic rules of operation. In this way, the optimized model performs the same calculations as an ordinary model, but uses less memory for the order parameter and solves $O(1)$ equations instead of $O(N_\mathrm{p})$ on each material point. Notably, since each particle has a unique phase index, no special cutoff range is required for the advection solving, as it is in [34]. The algorithm including the efficiency improvement methods is shown in Table. 1.

3 Performance tests

To test the performance of the model, we present several 2D test cases. The 2D geometries are initialized using triangle meshes. The nodes of the triangle mesh are directly used as the nodes in this model. The material points are initialized at the barycenters of the triangles.

3.1 Two symmetric particles sintering

The 2-D sintering of two equal particles with the same diameters is frequently used as a validation example of the model in previous works [32, 33, 35]. By modifying the diffusion potential coefficients D_vol, D_vap, D_surf, D_gb, different sintering patterns can be observed. The minimum global concentration potential is expected to form at the endpoints of the necking interface, leading to a transfer of concentration towards this region and causing an increase in the interface length. Because of the diffusion mechanism, the diffusion is likely to decrease as the local curvature reduces during this process. Analytical studies suggest that the neck length X and the initial diameter of the particles D follow the relation $\frac{X}{D}=Kt^c$, where $c<1$ is the exponent and K is the diffusion coefficient related to current material properties.

The diameter of the two particles is 40 nm. We discretize the computational domain into 9104 nodes and 17,830 material points. The logarithm results of test cases under different diffusion modes are shown in Fig. 3 and the concentration contours of $\rho=0.5$ are shown in Fig. 4. The coefficients are defined in Table. 2 same as defined in [32]. For all four cases, the results regress to a straight line very well, denoting that the necking obeys the analytical results. The case $T_\mathrm{vol+vap}$ and $T_\mathrm{vol+vap+gb}$ are close to each other, while the case $T_\mathrm{vol+vap+surf}$ and $T_\mathrm{vol+vap+gb+surf}$ are close to each other. This observation is coincident with Ref. [35], though the detailed forms of diffusion potentials are defined differently. The comparison of c and analytical value gain from Ref. [15] is shown in Table 3.

3.2 Nodal spacing test

In this section, different average nodal spacings are tested using the two particles sintering as the test case. The geometries of this section are initialized from uniform equilateral triangle meshes, with initial mesh sizes of 2.0, 1.5, 1.0, and 0.5 nm for the four respective cases. As the nodal spacing matches the mesh size in the equilateral triangle mesh, we label the cases based on their mesh sizes. The node counts for these cases are 1450, 2546, 5800, and 23,000, while the material points total 2744,

Table 1 Algorithm

Algorithm	
Step 1:	Set $n = 0$. Initialize nodal coordinates $x_{a,n}$, material point $x_{p,n}$, and neighborhood $N_H(x_p)$. Calculate the LME shape functions $N_a(x)$. Initialize nodal value η_a^n, ρ_a^n
Step 2:	Update the material points using $\eta_p^n(\alpha) = \sum_{a\in\mathcal{A}_p} \eta_a^n(\alpha) N_a(x_p)$, $\rho_p^n = \sum_{a\in\mathcal{A}_p} \rho_a^n N_a(x_p)$, $\nabla\eta_p^n(\alpha) = \sum_{a\in\mathcal{A}_p} \eta_a^n(\alpha) \nabla N_a(x_p)$, $\nabla\rho_p^n = \sum_{a\in\mathcal{A}_p} \rho_a^n \nabla N_a(x_p)$.
Step 3:	For every material point, do: If $\|\|\nabla\boldsymbol{\eta}_{p,n}\|\| < \epsilon_\eta$ and $\|\nabla\rho_{p,n}\| < \epsilon_\rho$ deactivate the material point, Else, activate the material point.
Step 4:	Second-order Runge–Kutta iteration: (a) Solve $\boldsymbol{\mathcal{F}}_{\eta,a}^n$ and $\mathcal{F}_{\rho,a}^n$ from Eqs. (20) and (21). (b) Solve $\boldsymbol{\eta}_a^{n+\frac{1}{2}} = \boldsymbol{\eta}_a^n + \frac{1}{2}\boldsymbol{\mathcal{F}}_{\eta,a}^n \Delta t$, and $\rho_a^{n+\frac{1}{2}} = \rho_a^n + \frac{1}{2}\mathcal{F}_{\rho,a}^n \Delta t$. (c) Update $\boldsymbol{\eta}_p^{n+\frac{1}{2}}$, $\rho_p^{n+\frac{1}{2}}$, $\nabla\boldsymbol{\eta}_p^{n+\frac{1}{2}}$, $\nabla\rho_p^{n+\frac{1}{2}}$. (d) Solve $\boldsymbol{\mathcal{F}}_{\eta,a}^{n+\frac{1}{2}}$ and $\mathcal{F}_{\rho,a}^{n+\frac{1}{2}}$ from Eqs. (20) and (21). (e) Update $\boldsymbol{\eta}_a^{n+1} = \boldsymbol{\eta}_a^{n+\frac{1}{2}} + \frac{1}{2}\boldsymbol{\mathcal{F}}_{\eta,a}^{n+\frac{1}{2}} \Delta t$, and $\rho_a^{n+1} = \rho_a^{n+\frac{1}{2}} + \frac{1}{2}\mathcal{F}_{\rho,a}^{n+\frac{1}{2}} \Delta t$.
Step 5:	Set $n = n + 1$. Go to Step 2 until the maximum number of iterations is reached.

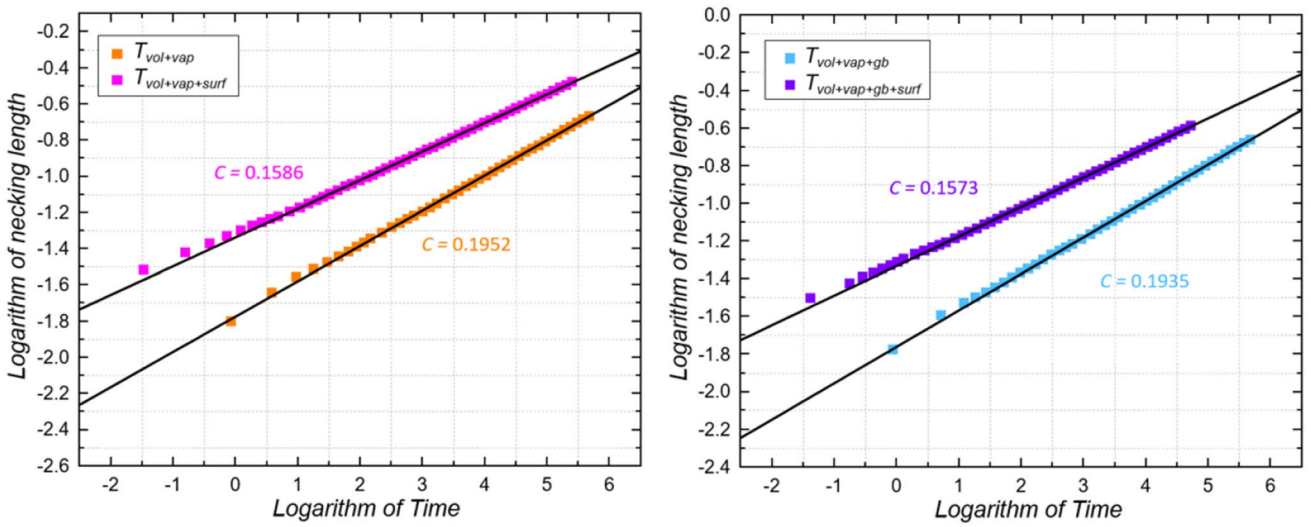

Fig. 3 The logarithm relation of necking length and time. All four test cases regress to a line. the values of c for different diffusion patterns are the regressed gradient

4884, 11,286, and 45,372. The particle diameter stands at 40 nm. The results are plotted in Fig. 5, from which the following observations are gained. The concentration profiles along the necking interface are converging as the averaging nodal spacing decreases. The interface is not well resolved for the 2.0 and 1.5 nm cases, leading to the deviated results from the small average nodal spacing cases.

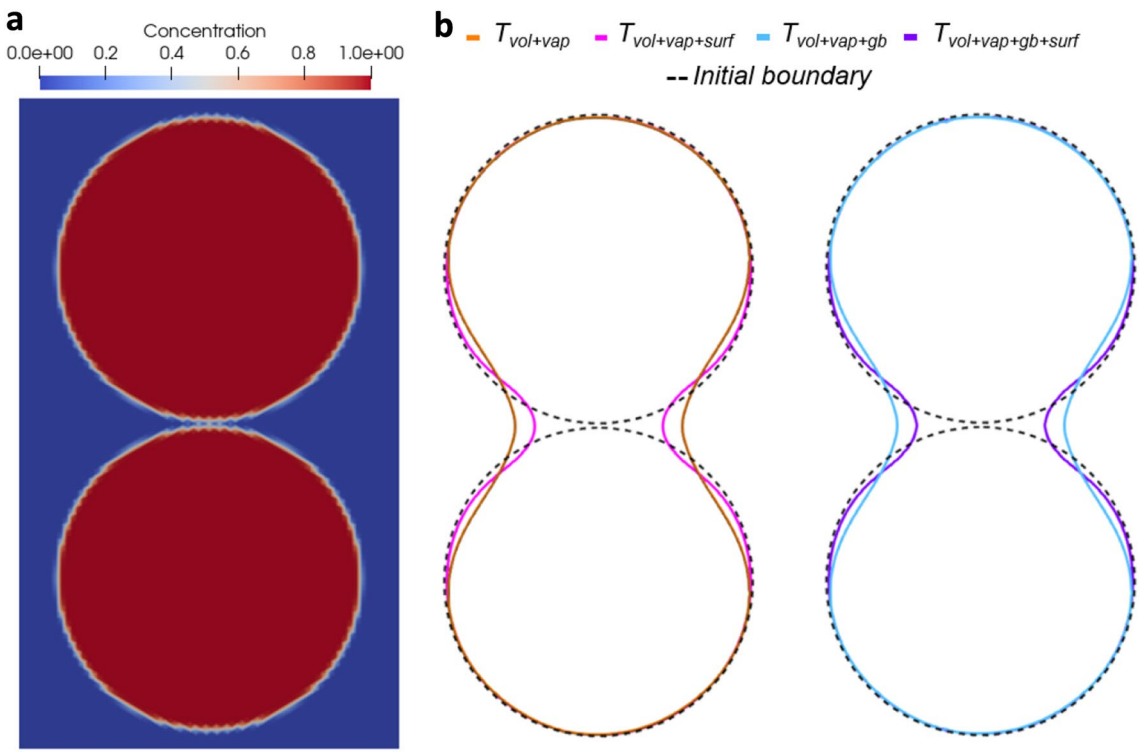

Fig. 4 **a** The initial concentration distribution of the symmetric particles sintering. **b** Contour line of $\rho = 0.5$ for different diffusion patterns

Table 2 Coefficients specification

Coefficients	Value
A	16.0
B	1.0
L	10.0
κ_ρ	10.0
κ_η	1.0
D_{gb}	0.4
D_{vol}	0.01
D_{surf}	4.0
D_{vap}	0.001
m_t	500.0
m_t	1.0
k	100.0
ρ_0	0.9816
c	0.14

Table 3 Simulation results and analytical values of neck growth exponent

	c	$1/c$	Analytical value of $1/c$
$T_{\text{vol+vap}}$	0.1952	5.1241	5
$T_{\text{vol+vap+gb}}$	0.1935	5.1670	6
$T_{\text{vol+vap+surf}}$	0.1586	6.3034	7
$T_{\text{vol+vap+gb+surf}}$	0.1573	6.3572	–

3.3 Search range test

Recall the form of nodal search range of the LME shape function which is $h_a = h\sqrt{-\log(\delta_0)\gamma_a}$, where the coefficient h is an adjustable value. The choice of h decides the nodes-material points connectivity table, but the results should not be sensitive to the choice of h. The symmetric sintering example is initialized with different values of h and FEM. The contour lines of concentration $\rho = 0.5$ at $t = 50$ for all the test cases are shown in Fig. 6. The coincidence of the contour lines indicates that changing the value of h did not affect the solution significantly. The exponential coefficient c obtained from the FEM case is 0.1576, and for $h = 1.0, 5.0$ and 10.0, it is 0.1573, 0.1607 and 0.1607, respectively.

Based on the result from Sect. 3.2, for the best performance and computation efficiency, we suggest that the average nodal spacing and the search range should both be set values close to the interface thickness. The thickness can be estimated using the following equation [50]:

$$l_{\text{interf}} = \frac{1}{|\mathrm{d}\eta_\alpha/\mathrm{d}x|_{x=0}} = \sqrt{\frac{f_{\text{interf}}}{\kappa_\eta}}, \tag{33}$$

where f_{interf} is the value of f in the interfaces. The estimated value is 0.9014 for this work. Notice that rather than a strict

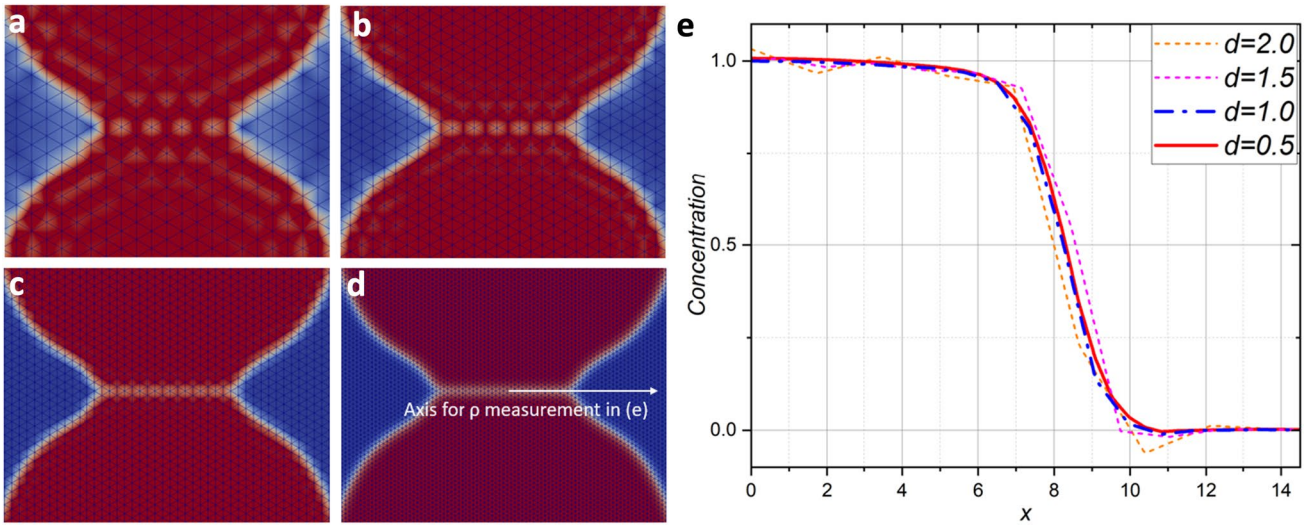

Fig. 5 The results at $t = 10$. **a**–**d** $|\eta|$ distribution and nodal configuration at the necking area for varying average nodal spacing: **a** 2.0, **b** 1.5, **c** 1.0, and **d** 0.5. **e** The concentration distribution along the necking interface starting from the center point of the interface

criterion, the estimation serves merely as a guiding point. The nodal distance and search range are tuned to give desirable resolution while maintaining acceptable computational expenses.

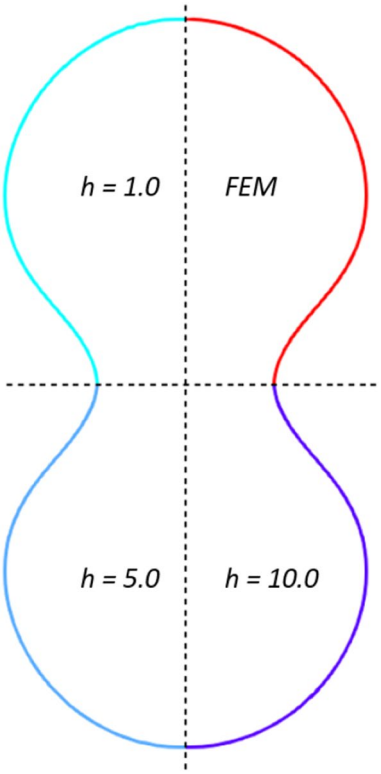

Fig. 6 The contour line of concentration $\rho = 0.5$ at $t = 50$ for the FEM and $h = 1.0, 5.0$, and 10.0, respectively

3.4 Two uneven particles sintering

When two particles with a significant size difference undergo sintering, concentration transfers from the smaller particle to the larger particle due to the diffusion mechanism. As a result, the volume of the smaller particle decreases, eventually leading to complete merging with the larger particle. The test case was initiated with two particles of diameter 20 nm and nm. The geometry employed is the same as the first test case. Figure 7 displays the shapes of the particles at different time intervals, clearly showing the merging of the smaller particle into the larger one. The area curve demonstrates that the rate of decrease is higher at the beginning and end of the process, with a relatively slower rate during the intermediate period, which is consistent with the findings reported in Ref. [33].

3.5 Mesh sensitivity test

The performance of the traditional FEM is limited by the meshing quality. Moreover, the solution of the FEM phase-field model can be interfered with by the meshing pattern even if the geometry is a structured regular mesh [37]. While reducing mesh size can decrease mesh sensitivity, it also increases computational costs, particularly for large-scale simulations. However, the current model updates the connectivity table based on the search range and weights of the LME shape function, making it feasible to work with even very low-quality local meshes. Here we investigate the effects of different mesh quality on the simulation results between FEM and the proposed approach. As a test case, the spheroidization of a single square particle is used, where the square particle gradually becomes round due to decreasing

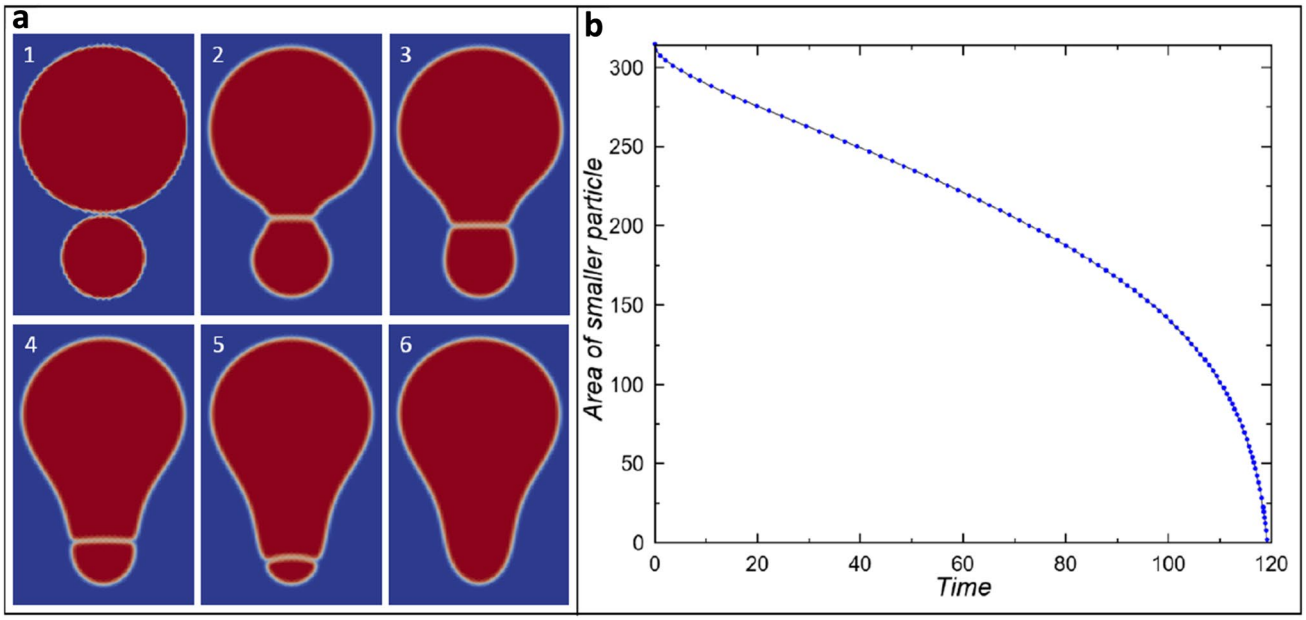

Fig. 7 **a** Distribution of $|\eta| = \sum_{\alpha}(\eta(\alpha))^2$ of the uneven particles sintering at $t = 0, 5, 30, 100, 115, 120$, respectively. **b** Area of smaller particle versus time

surface energy. We use three different meshes as the mesh for FEM as well as to initialize the nodes and material points in the proposed approach. One mesh is uniform, the other two are ill-conditioned. It is important to note that geometry meshing is only used as input to initialize material points and nodes [39, 48]. The geometry of the uniform nodal configuration case consists of 1840 nodes and 3510 material points. Meanwhile, the two ill-conditioned nodal configuration cases involve 3600 and 3225 nodes, along with 6962 and 6068 material points, respectively.

Figure 8 displays the result obtained using a regular nodal configuration, where the spheroidization of the square particle is clearly observed. Figure 9 demonstrates cases with the same initial concentration distribution but different nodal configuration. The elements in the initialization meshes are ill-shaped with small Jacobian. The meshfree model accurately simulates the process, producing the correct result as the regular nodal configuration. However, the FEM cases do not converge due to the low meshing quality. The final diameters of the regular mesh case, pattern 1 case, and pattern 2 case are 17.562, 17.671, and 17.672 nm, respectively, with a relative error of less than 0.5%. The values are calculated from the horizontal and vertical measurement of contour $\rho = 0.5$.

The five tests conducted above confirm that this meshfree phase-field model is accurate and robust. It is able to solve problems even if the initial input geometry is very

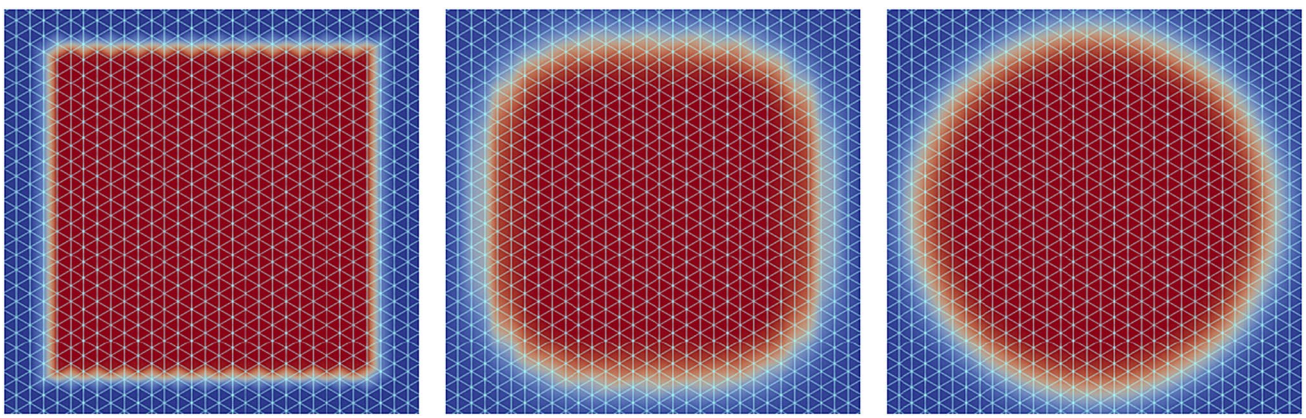

Fig. 8 Spheroidization initialized using a fine regular mesh

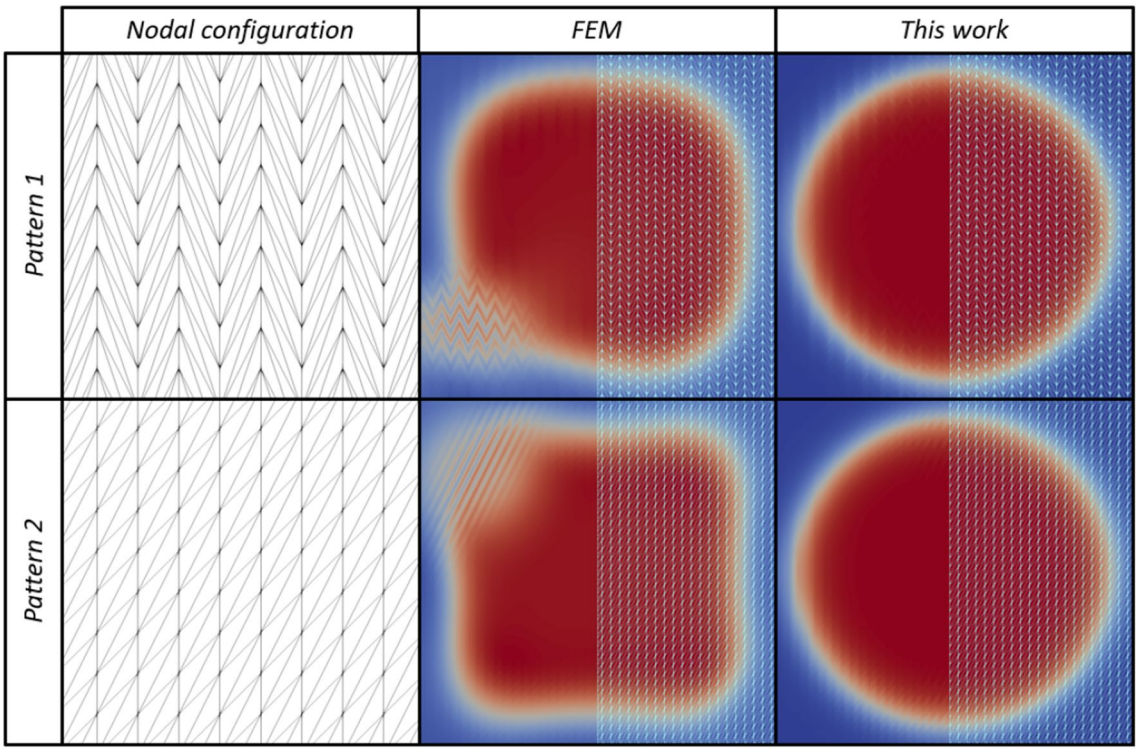

Fig. 9 Result initialized using different nodal configuration. The FEM tests are not converging. The meshfree model is giving the correct result

irregular, with which the FEM fails. Therefore, the model has been successfully validated.

4 Simulation results

For the sintering model, the results are much more validated in large simulation cases. In this work, one 2D case and four 3D cases are studied. The coefficients used for all of the cases are decided based on Wang's work [32] which ensures a physically meaningful ratio of different types of diffusions. They are shown in Table 2. The geometry for 2D case is initialized using triangle mesh, while the counterpart of 3D case is initialized from tetrahedron mesh. The mesh nodes are taken as the nodes for this model, and the material points are initialized at the barycenters of the elements. The initial geometry is generated with a DEM code, in which particles have linear contact forces filling into given shape containers. After the DEM simulation is done, the initial value of concentration and order parameters are assigned for each particle using the same approach in Ref. [34] as

$$\eta(\boldsymbol{r},\alpha)=\frac{1}{2}\left(1-\tanh\left(\frac{d(\alpha)-R(\alpha)}{\xi}\right)\right),\quad \rho=\sum_{\alpha}\eta(\alpha), \tag{34}$$

where $d(\alpha)$ is the distance between the current position and the α-th particle, $R(\alpha)$ denotes the radius of the particle, and ξ is a boundary thickness coefficient which is picked to make the initial boundary thickness reasonable. The value of ξ is 1.0 in the work.

Some observations are shared among all the results both in 2D and 3D. The early stage necking is observed, i.e., the interface area rapidly increases while the sharp concave or convex area disappears. After that in the steady sintering stage, the inner vacancy area becomes spherical or nearly spherical, then gradually decreases to zero. The vacancy ratio, a parameter denoting the volumetric fraction of vacancy inside the fabricated structure, has been computed for all the scenarios presented in this study. The methodology employed to solve for the vacancy ratio draws inspiration from the approach outlined in Ref. [34]. To determine the vacancy ratio, a defined box area within the particle pack, with a volume of V_{box}, is considered. The vacancy ratio, denoted as R_v, is then calculated using the equation:$R_v = 1 - \int_{\Omega_{\text{box}}} \rho \mathrm{d}v / V_{\text{box}}$. The dimensions and placement of this box are strategically chosen to maximize its volume while ensuring complete coverage within the particle pack during the sintering process. This ensures that the computed vacancy ratio is representative of the entire system's behavior and characteristics.

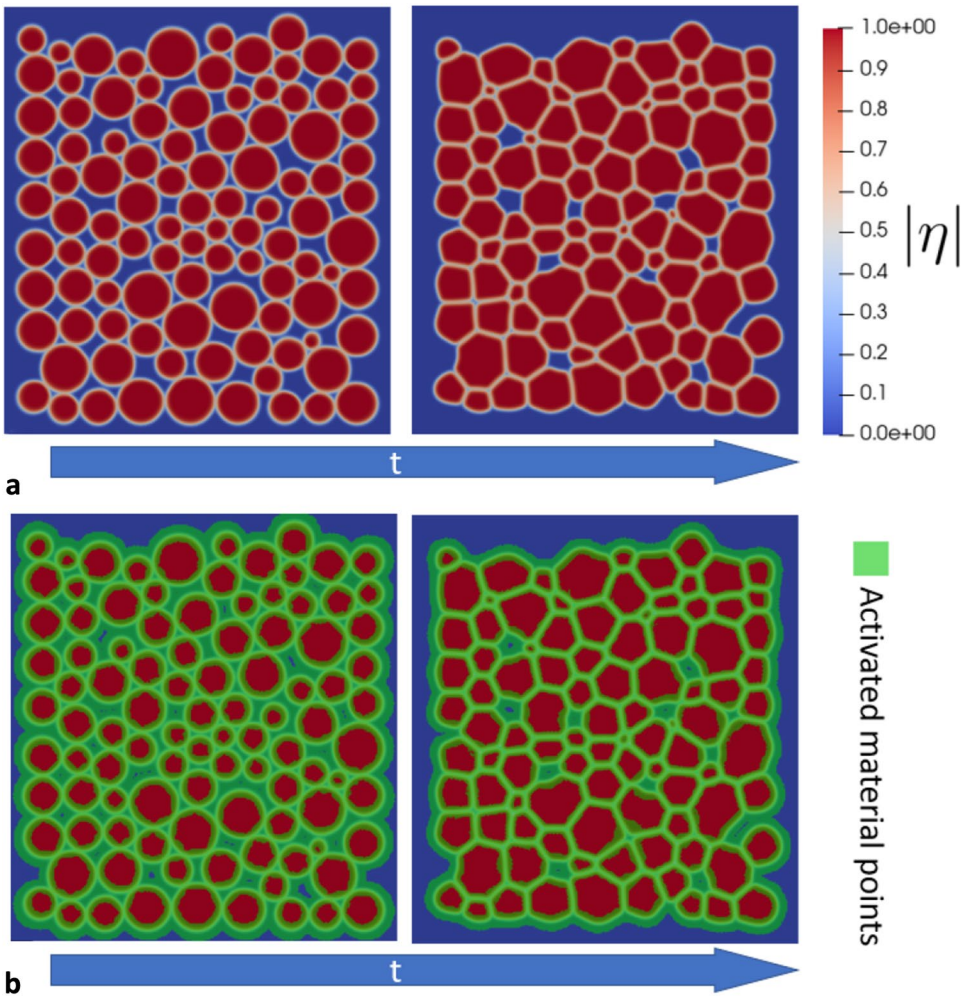

Fig. 10 Results of the 2D case $t = 0.0$ and $t = 5.0$. **a** The contour plot of the norm of order parameters $|\boldsymbol{\eta}|$. Merging of the particles and forming of the interfaces can be observed. **b** The material points are activated along the boundary and interfaces

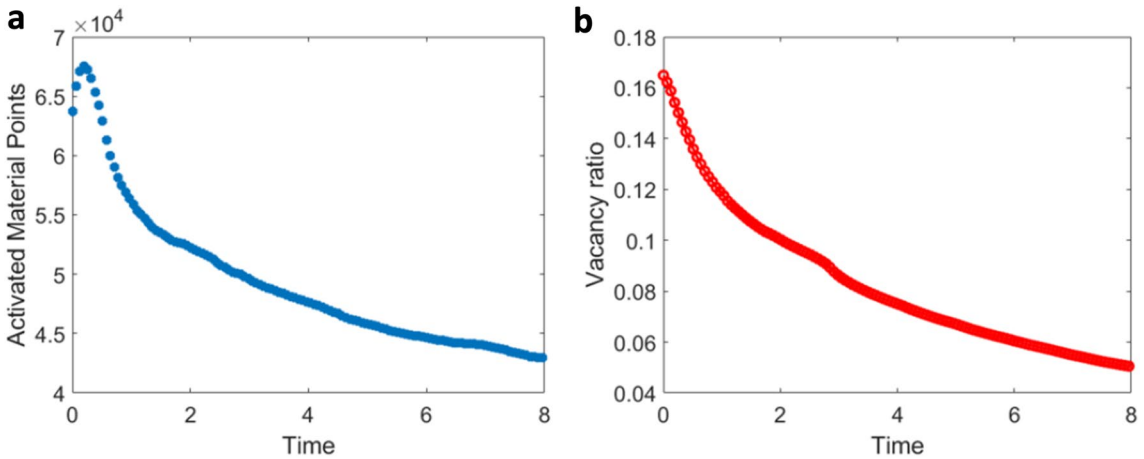

Fig. 11 Number of activated material points and vacancy ratio of the 2D case versus time. The number of activated material points decreases because the system energy is decreasing and the activated material points are tracking the surface and interface

Parallel solving is implemented using OpenMPI. The processors being used are Intel Xeon Gold 6134 for all the cases. The number of cores being used is 5 for the 2D case and 30 for all the 2D cases.

4.1 2D case

A 2D case is used to test the model's capability of solving the 2D problems and clearly show the optimized approaches.

100 particles are initiated in a 105 nm × 125 nm box. The total number of nodes is 53,889 and the number of material points is 106,848. The box used to calculate the vacancy ratio is a square centered at the geometry with side length equal to 80 nm. In Fig. 10, the development of order parameters as well as the activated material points is shown. The merging and necking of the particles and forming of dihedral angles are observed. The activated material points distribution is marked using the green area in the figures. The activation threshold for the material points is set as $\epsilon_\eta = 0.00001, \epsilon_\rho = 0.00001$. As expected, the activated material points are tracking the interfaces and the particle boundaries. In addition, the total number of the activated material points decreases over time, for the boundary and interface area is decreasing with the system free energy.

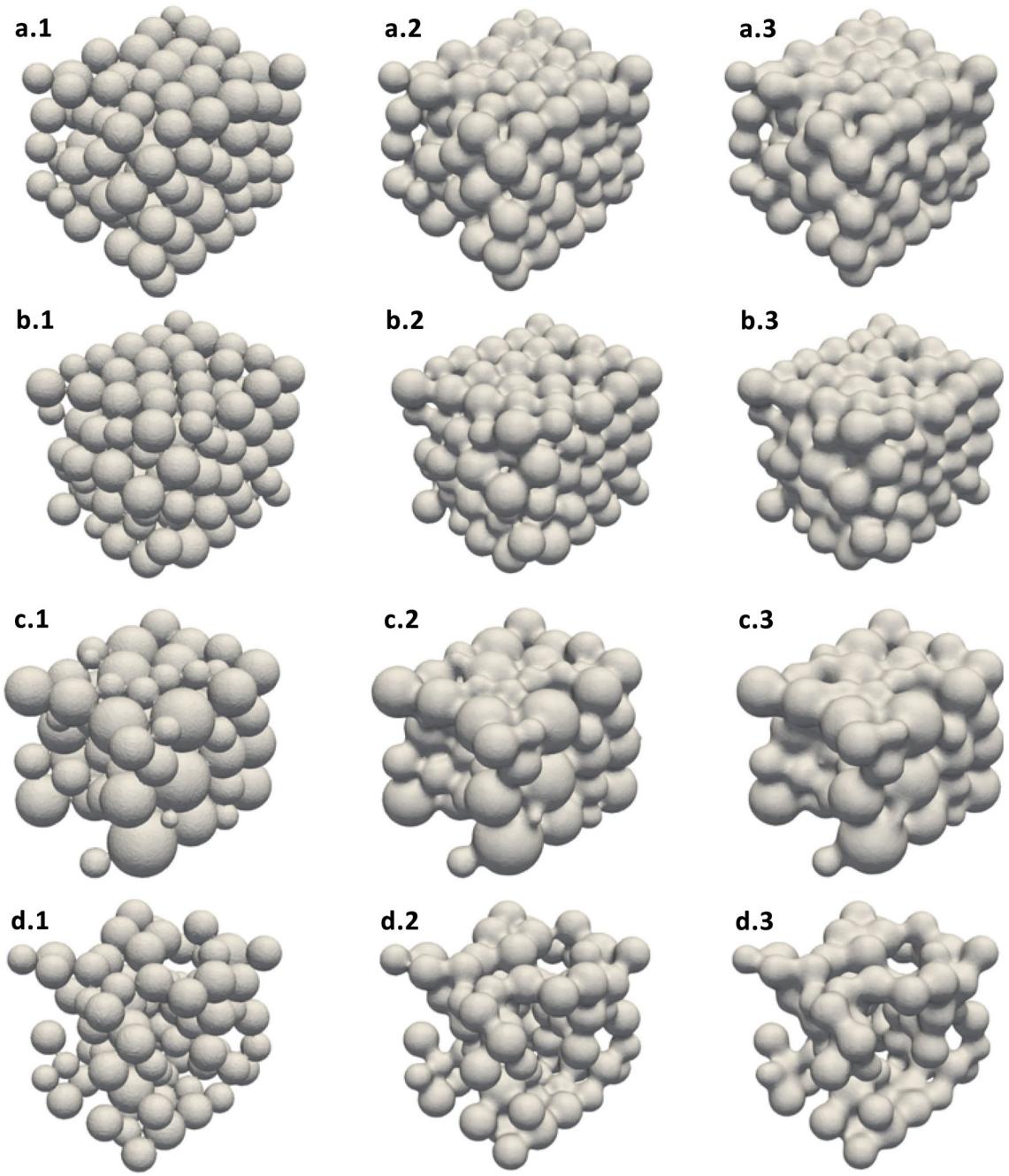

Fig. 12 Contour of concentration $\rho = 0.5$. The index **a**–**d** denote Case A, B, C, and D, respectively. In addition, the number 1, 2 and 3 denote simulation time $t = 0.0$, $t = 5.0$ and $t = 15.0$. Case A, B, and D are using the same average particle diameter and variance, while the variance of case C is larger

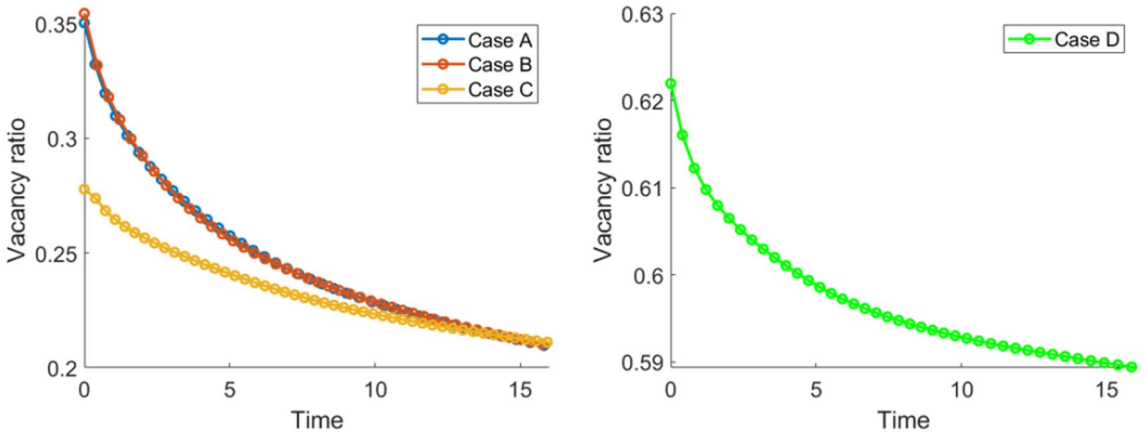

Fig. 13 Vacancy ratio versus time for 3D cases A, B, C, and D. Case A and B are coincident with each other

The total number of degrees of freedom is 5,442,789. With all the efficiency improvement methods off, the simulation took 1118 min, while the time taken for the optimized scenario is 108 min, which is almost 10 times faster. The relative difference $\epsilon = \frac{\sum_a |\rho_{0,a} - \rho_{opt,a}|}{\sum_a |\rho_{0,a}|}$ is less than 0.0014 for all the output results, where $\rho_{0,a}$ and $\rho_{opt,a}$ are the nodal concentration for cases with efficiency improvement off and on, respectively. Therefore, we claim that the efficiency improvement method is validated (Fig. 11).

4.2 3D cases

The computational domain is a 100 nm × 100 nm × 125 nm box, consisting of 5,132,460 material points and 942,587 nodes. The box used for vacancy ratio solving is a cube with side length equal to 80 nm placed at the center of the geometry. The initiation of particles is solved from a DEM scheme giving compact packing of point-contacting spheres. There are collectively four cases provided. Case A, B, and D are initiated using spheres with mean radius $R_{\text{ave}} = 10.0$ nm and standard difference $\sigma = 1.0$. Case C is initiated with $R_{\text{ave}} = 12.0$ nm and $\sigma = 3.0$ for testing different particle size distributions. The initial vacancy ratio of case A, B, C, and D are, respectively, 0.351, 0.350, 0.277, 0.621. In addition, the numbers of particles are 143, 150, 134, and 85 for case A, B, C and D, respectively.

Figure 12 shows the contour of concentration $\rho = 0.5$ for the cases at different times. The necking between particles and the overall shrinkage of the geometry is well observed. Case A and B are initialed with the same distribution setting, i.e., the same average radius and standard difference, to check if the model is reacting consistently to similar input. The initial vacancy ratios are very close. In addition, the development of vacancy ratios are coincident with each other as expected. Case C is initialized using radius distribution with a larger standard variation. The complete absorption of small particles into large ones is observed. In addition, the steady sintering stage is reached earlier than in case A and B and the sintering efficiency is lower. For case D, the initial vacancy ratio is lower than in the three other cases. From the contour plot, it is observed that the particles aggregate locally instead of moving toward the overall geometric center, resulting in a low vacancy ratio decreasing rate and not asymptotically converging to zero (Fig. 13).

5 Conclusion

In conclusion, we have presented a meshfree scheme that effectively solves the rigid body motion included in the particle sintering phase-field problem. Our use of the LME shape functions based on the material points framework as a spatial discretization scheme has proven to be reliable, and we have developed two efficiency improvement methods to enhance the accuracy and efficiency of the simulation. Five performance test examples are conducted to demonstrate the accuracy of the model and its ability to solve problems even with initial geometries that cause the FEM to fail. Our observations of sintering behaviors in both 2D and 3D cases aligned with different stages of real-world processes. Specifically, in the 2D case, we clearly showed the area occupied by activated material points, which decreased as the simulation entered the steady sintering stage. In the 3D case, we observed shrinkage and merging, and the vacancy ratio decreased faster for larger initial packing rates. We also found that for loose cases, the vacancy ratio did not converge to zero. Moving forward, we recommend two possible future development directions for this model. One direction involves implementing a fully thermomechanical coupling under

the HOTM framework, where the total system free energy is related to the phase field, temperature, and deformation simultaneously. Furthermore, since the proposed model presents accurate and stable solutions for the phase-field sintering problems that consist of both the Allen–Cahn equation and the Cahn–Hillard equation, it is promising that the proposed framework can be employed to address other phase-field problems. Moreover, the efficiency enhancement techniques proposed in this study are also applicable for other problems. Potential models that could benefit from the proposed approach encompass the grain growth models, dendritic growth models, membrane models, and multi-phase flow models, which will be taken into account in the future.

Acknowledgements This work was supported by USDA-NIFA (2021-67021-33998) and Case Western Reserve University.

Data availability Not applicable.

Declarations

Conflict of interest The authors declare that they have no conflicts of interest.

References

1. Cao C, Andrews JB, Franklin AD (2017) Completely printed, flexible, stable, and hysteresis-free carbon nanotube thin-film transistors via aerosol jet printing. Adv Electron Mater 3(5):1700057
2. Cao C, Andrews JB, Kumar A, Franklin AD (2016) Improving contact interfaces in fully printed carbon nanotube thin-film transistors. ACS Nano 10(5):5221–5229
3. Catenacci MJ, Flowers PF, Cao C, Andrews JB, Franklin AD, Wiley BJ (2017) Fully printed memristors from cu-sio2 core-shell nanowire composites. J Electron Mater 46(7):4596–4603
4. Pang Y, Cao Y, Chu Y, Liu M, Snyder K, MacKenzie D, Cao C (2020) Additive manufacturing of batteries. Adv Funct Mater 30(1):1906244
5. Chu Y, Qian C, Chahal P, Cao C (2019) Printed diodes: materials processing, fabrication, and applications. Adv Sci 6(6):1801653
6. Wang L, Zhenning W, Cao C (2019) Technologies and fabrication of intelligent packaging for perishable products. Appl Sci 9(22):4858
7. Tian B, Fang Y, Liang J, Zheng K, Guo P, Zhang X, Youfusheng W, Liu Q, Huang Z, Cao C et al (2022) Fully printed stretchable and multifunctional e-textiles for aesthetic wearable electronic systems. Small 18(13):2107298
8. Zhou Y, Parker CB, Joshi P, Naskar AK, Glass JT, Cao C (2021) 4d printing of stretchable supercapacitors via hybrid composite materials. Adv Mater Technol 6(1):2001055
9. Garanger K, Feron E, Garoche P-L, Rimoli JJ, Berrigan JD, Grover M, Hobbs K (2017) Foundations of intelligent additive manufacturing. arXiv preprint arXiv:1705.00960
10. Smith J, Xiong W, Yan W, Lin S, Cheng P, Kafka OL, Wagner GJ, Cao J, Liu WK (2016) Linking process, structure, property, and performance for metal-based additive manufacturing: computational approaches with experimental support. Comput Mech 57:583–610
11. Svoboda J, Riedel H, Zipse H (1994) Equilibrium pore surfaces, sintering stresses and constitutive equations for the intermediate and late stages of sintering-i. computation of equilibrium surfaces. Acta Metall Mater 42(2):435–443
12. Coble RL (1961) Sintering crystalline solids. I. Intermediate and final state diffusion models. J Appl Phys 32(5):787–792
13. Fang ZZ (2010) Sintering of advanced materials. Elsevier, Amsterdam
14. Ashby MF (1974) A first report on sintering diagrams. Acta Metall 22(3):275–289
15. German RM (1996) Sintering theory and practice. John Wiley & Sons Inc., New York
16. German RM, Lathrop JF (1978) Simulation of spherical powder sintering by surface diffusion. J Mater Sci 13(5):921–929
17. Bouvard D, McMeeking RM (1996) Deformation of interparticle necks by diffusion-controlled creep. J Am Ceram Soc 79(3):666–672
18. Pan J, Cocks ACF, Kucherenko S (1997) Finite element formulation of coupled grain-boundary and surface diffusion with grain-boundary migration. Proc Roy Soc Lond Ser A Math Phys Eng Sci 453(1965):2161–2184
19. Pan J, Le H, Kucherenko S, Yeomans JA (1998) A model for the sintering of spherical particles of different sizes by solid state diffusion. Acta Mater 46(13):4671–4690
20. Singh R, Sharma V (2022) Investigations on sintering mechanism of nano tungsten carbide powder based on molecular dynamics simulation and experimental validation. Adv Powder Technol 33(9):103724
21. Singh R, Sharma V (2021) Nano tungsten carbide interactions and mechanical behaviour during sintering: a molecular dynamics study. Comput Mater Sci 197:110653
22. Wang F, Tang Z, He H (2018) Stress-dislocation interaction mechanism in low-temperature thermo-compression sintering of Ag NPs. AIP Adv 8(4):045012
23. Grouchko M, Roitman P, Zhu X, Popov I, Kamyshny A, Haibin S, Magdassi S (2014) Merging of metal nanoparticles driven by selective wettability of silver nanostructures. Nat Commun 5(1):1–6
24. Sestito JM, Abdeljawad F, Harris TAL, Wang Y, Roach A (2019) An atomistic simulation study of nanoscale sintering: the role of grain boundary misorientation. Comput Mater Sci 165:180–189
25. Matsuda T (2021) Development of a dem taking account of neck increments caused by surface diffusion for sintering and application to analysis of the initial stage of sintering. Comput Mater Sci 196:110525
26. Nosewicz S, Rojek J, Pietrzak K, Chmielewski M (2013) Viscoelastic discrete element model of powder sintering. Powder Technol 246:157–168
27. Wünscher S, Rasp T, Grouchko M, Kamyshny A, Paulus RM, Perelaer J, Kraft T, Magdassi S, Schubert US (2014) Simulation and prediction of the thermal sintering behavior for a silver nanoparticle ink based on experimental input. J Mater Chem C 2(31):6342–6352
28. Wang X, Atkinson A (2018) Combining densification and coarsening in a cellular automata-Monte-Carlo simulation of sintering: methodology and calibration. Comput Mater Sci 143:338–349
29. Bordère S, Bernard D (2008) Full resolution of the Monte Carlo time scale demonstrated through the modelling of two-amorphous-particles sintering. Comput Mater Sci 43(4):1074–1080
30. Qiu F, Egerton TA, Cooper IL (2008) Monte Carlo simulation of nano-particle sintering. Powder Technol 182(1):42–50
31. Jing XN, Zhao JH, He LH (2003) 2d aggregate evolution in sintering due to multiple diffusion approaches. Mater Chem Phys 80(3):595–598

32. Wang YU (2006) Computer modeling and simulation of solid-state sintering: a phase field approach. Acta Mater 54(4):953–961
33. Chockalingam K, Kouznetsova VG, van der Sluis O, Geers MGD (2016) 2d phase field modeling of sintering of silver nanoparticles. Comput Methods Appl Mech Eng 312:492–508 (**Phase Field Approaches to Fracture**)
34. Termuhlen R, Chatzistavrou X, Nicholas JD, Hui-Chia Yu (2021) Three-dimensional phase field sintering simulations accounting for the rigid-body motion of individual grains. Comput Mater Sci 186:109963
35. Hötzer J, Seiz M, Kellner M, Rheinheimer W, Nestler B (2019) Phase-field simulation of solid state sintering. Acta Mater 164:184–195
36. Tonks MR, Gaston D, Millett PC, Andrs D, Talbot P (2012) An object-oriented finite element framework for multiphysics phase field simulations. Comput Mater Sci 51(1):20–29
37. Wang HY, Li R (2008) Mesh sensitivity for numerical solutions of phase-field equations using R-adaptive finite element methods. Commun Comput Phys 3(2):357–375
38. Liu G-R, Liu MB (2003) Smoothed particle hydrodynamics: a meshfree particle method. World Scientific, Singapore
39. Wang H, Liao H, Fan Z, Fan J, Stainier L, Li X, Li B (2020) The hot optimal transportation meshfree (HOTM) method for materials under extreme dynamic thermomechanical conditions. Comput Methods Appl Mech Eng 364:112958
40. Fan Z, Li B (2019) Meshfree simulations for additive manufacturing process of metals. Integr Mater Manuf Innov 8(2):144–153
41. Fan Z, Wang H, Huang Z, Liao H, Fan J, Jian L, Liu C, Li B (2021) A Lagrangian meshfree mesoscale simulation of powder bed fusion additive manufacturing of metals. Int J Numer Methods Eng 122(2):483–514
42. Jiang H, Wang H, Scott V, Li B (2022) Numerical analysis of oblique hypervelocity impact damage to space structural materials by ice particles in cryogenic environment. Acta Astronaut 195:392–404
43. Wang H, Li X, Phipps M, Li B (2022) Numerical and experimental study of hot pressing technique for resin-based friction composites. Compos A Appl Sci Manuf 153:106737
44. Arroyo M, Ortiz M (2006) Local maximum-entropy approximation schemes: a seamless bridge between finite elements and meshfree methods. Int J Numer Methods Eng 65(13):2167–2202
45. Fan J, Liao H, Wang H, Junheng H, Chen Z, Jian L, Li B (2018) Local maximum-entropy based surrogate model and its application to structural reliability analysis. Struct Multidiscipl Optim 57:373–392
46. Amiri F, Millán D, Shen Y, Rabczuk T, Arroyo M (2014) Phase-field modeling of fracture in linear thin shells. Theor Appl Fract Mech 69:102–109
47. Rosolen A, Peco C, Arroyo M (2013) An adaptive meshfree method for phase-field models of biomembranes. Part I: approximation with maximum-entropy basis functions. J Comput Phys 249:303–319
48. Li B, Habbal F, Ortiz M (2010) Optimal transportation meshfree approximation schemes for fluid and plastic flows. Int J Numer Methods Eng 83(12):1541–1579
49. Lee J, Jeong S (2017) Stability of finite difference schemes on the diffusion equation with discontinuous coefficients. Massachusetts Institute of Technology, Cambridge
50. Moelans N, Blanpain B, Wollants P (2008) Quantitative analysis of grain boundary properties in a generalized phase field model for grain growth in anisotropic systems. Phys Rev B 78(2):024113